

# Design and Performance Analysis of a Repeater-Assisted Multireceiver Wireless Power Transfer System Operating at MHz Frequencies

YINING LIU <sup>1</sup>, NAM HA-VAN <sup>2</sup> (Member, IEEE), PRASAD JAYATHURATHNAGE <sup>1,3</sup> (Senior Member, IEEE),  
JORMA KYRÄ <sup>1</sup> (Member, IEEE), AND SERGEI A. TRETYAKOV <sup>2</sup> (Fellow, IEEE)

<sup>1</sup>Department of Electrical Engineering and Automation, Aalto University, 00076 Espoo, Finland

<sup>2</sup>Department of Electronics and Nanoengineering, Aalto University, 00076 Espoo, Finland

<sup>3</sup>Danfoss Drives, 33560 Tampere, Finland

CORRESPONDING AUTHOR: YINING LIU (e-mail: yining.1.liu@aalto.fi).

**ABSTRACT** Simultaneous wireless power transfer (WPT) to multiple receivers (Rxs) is an important requirement for wireless charging of consumer electronic devices. In this article, we propose a WPT coil structure capable of achieving independent multi-Rx WPT with a confined and uniform rotating magnetic field at megahertz operating frequencies. Compared with the existing multiple receiver WPT structures, the proposed structure exhibits low leakage flux outside the power transmitter. Thanks to the single-coil transmitter structure and the load-independent current feature in the repeater coil, no additional control circuit is needed to obtain independent power transfer to multiple receiver devices. The proposed solution is experimentally demonstrated in a 6.78-MHz 80-W WPT prototype, with a dc-to-dc efficiency of 90.2 % in the full-load case using four 20-W receiver circuits.

**INDEX TERMS** Confined magnetic field, multiple receivers, megahertz (MHz), parasitic effects, wireless power transfer (WPT).

## I. INTRODUCTION

Wireless power transfer (WPT) techniques have gained significant popularity in recent years, finding widespread applications in consumer electronic and portable devices. These applications have generated increasing demands for enhanced charging freedom, efficiency, and safety, in particular, the need for ensuring conformity to the specific absorption rate limitations.

In pursuit of these objectives, various WPT coil structures have been proposed as alternatives to the conventional spiral-type coils. Good misalignment tolerance [1] and large positional freedom can be realized by novel coil designs on either the transmitter (Tx) or the receiver (Rx) side. In [2], [3], and [4], multicoil Rx arrangements are proposed to achieve both positional and rotational freedom within a planar-type transmitting area. Similarly, through new Tx designs with combinations of multiple coils [5], [6], [7], Rx coils can

achieve 2-D or 3-D charging freedom with a simple spiral structure.

The diverse free-positional WPT link structures offer high potential for simultaneous charging of multiple receivers, which was not explored in the aforementioned works. To realize concurrent charging of multiple receivers, previous works, such as [8], [9], and [10] focused on employing multiple frequency channels, with each Rx circuit tuned to a distinct resonance frequency. However, the number of Rxs that can be charged simultaneously is restricted by the number of different frequency channels and the frequency-selective performance of the compensation networks on the transmitter side. For example, in [10], despite designing up to six resonance frequency channels, simultaneous power transfer was still limited to only two Rxs. In [11], multiple relays were used to realize long-distance multiple-receiver WPT, while the power transfers to the Rxs are not independent from each

other. On the other hand, large-area multi-Rx WPT was realized in [12] with a planar transmitter. A complex excitation current modulation strategy was needed to generate a 3-D rotating magnetic field.

A bowl-shaped [13], [14] and a ball-shaped [15], [16] Tx structures have been proposed to achieve free-positional multi-Rx WPT. In both cases, the transmitter is composed by multiple coils connected to separate power supplies, requiring complicated excitation current modulation or directional/rotational control methods. Further considerations regarding efficiency or load-independence requirements are investigated for the ball-shaped WPT systems. The authors in [17] focused on a maximum-efficiency tracking and power allocation method for multiple Rx's, while a self-tuning omnidirectional WPT was realized in [18] by introducing additional repeater coils. However, blind spots may easily form in the ball-shaped multicoil WPT systems, where the free-position characteristics are usually reached by dynamically controlling the amplitude or phase of the coil supplies. Full positional freedom is not possible when multiple Rx's are present in the charging area. To obtain a uniform magnetic field for coupling with multiple Rx coils, a single-Tx-coil cylindrical WPT structure was proposed in [19], where full 2-D multi-Rx WPT could be realized without the need for any control method.

Nevertheless, all the aforementioned structures, such as the planar, cylindrical, bowl-shaped, or ball-shaped coils, suffer from the problem of leakage flux. This means that the magnetic field generated by the transmitter broadly spreads into the surrounding space. The field leakage can pose safety concerns and adversely affect coupling between Tx and Rx's.

On the other hand, operating at a high frequency offers benefits of improved spatial freedom and compactness in circuit design [13], [22]. Frequencies up to several hundred kilo-hertz (kHz) or even mega-hertz (MHz) have been widely used to obtain robust coupling between air-core coils which have more benefits compared to the conventional couplers using bulky and costly ferrite cores. Regarding the low coupling coefficient  $k$  with air-core coils, operations in MHz frequency range can easily compensate its negative effect to the WPT efficiency since the quality factor  $Q$  is greatly improved in the MHz range [23]. However, increasing operating frequency also brings limitations to the system performance, especially with regard to parasitic parameters, which are no longer negligible at MHz frequencies [13], [22]. Thorough considerations of parasitic effects reveals importance of ensuring design accuracy and optimizing the system performance. When considering simultaneous power transfer to multiple Rx's, interference between load devices also becomes an important issue to be taken into account [24], [25].

In this article, we propose a novel multi-Rx WPT structure with a confined magnetic field. We aim to realize the basic functions of multi-Rx charging with the minimum requirement on control. The proposed air-core structure is formed by a helical Tx coil, a repeater (Rp), and simple planar spiral-shaped Rx coils. With the help of torus-wounded Rp

turns in a symmetrical geometry, the rotating toroidal field is confined inside the torus, resulting in uniform and strong coupling with Rx's at any position inside the torus. Such features make the structure suitable for simultaneous multi-Rx charging applications, such as small electronic devices including cellphones or tablets. Since only a single coil is used for the Tx, and the Rp coil provides load-independent current, no control circuitry is needed. Only series compensation capacitor is used for the proposed coils, therefore, there is no need for additional compensation inductors with ferrite core material as in high-order compensation circuits. The proposed concept of a uniform and confined magnetic field of the Tx device is verified by simulations. In addition, a comprehensive investigation of parasitic effects is made, targeting design accuracy and load-independent output performance. We choose to present a demonstration design for 6.78 MHz fix-frequency operations, which is also used as the working frequency in the *Airfuel Resonant* [26] WPT standard. A WPT system with four Rx's is built as an experimental prototype, with each Rx loaded to receive around 20 W of power. The system provides 90.2 % dc-to-dc efficiency at the full load.

In terms of the design target and performance, the WPT system with our proposed coil structure is compared with several existing multi-Rx WPT systems in Table 1. With the target of multi-Rx charging, using the traditional spiral-type-based coils always results in a rapid increase in either Tx size [20], [27] or the amount of Tx coils [21], due to their weak coupling at misaligned positions. Combining the coils in series or parallel to use one common converter and tuning circuit [20] reduces the charging flexibility, more specifically, it creates blind zones where the Rx could not get power. However, having individual Tx-coil control can only solve the blind zone issue for single-Rx charging applications [18] by actively shifting them to another position in the charging space. Neither ON/OFF nor active phase control will help when the second Rx happens to be located at the new blind-zone position shifted due to the control for first Rx. Moreover, the magnetic fields in all these designs are shaped by several Tx coils together. Such field combining methods easily lead to an uneven distribution of field, results in high fluctuations in power delivery at different Rx positions. In comparison, the proposed structure does not suffer from any of these drawbacks since only one Tx-Rp pair is used. Meanwhile, the toroidal part of the Rp structure can generate a uniformly distributed magnetic field simultaneously for every position inside the 2-D torus without the presence of any blind zone or even weak zone for power transfer.

In terms of the possible options to reduce magnetic leakage, all the conventional designs in Table 1 spread out the flux to surroundings of the transmitting structure to enable charging freedom. Dynamic Rx-position detection and control are necessary for [21] to minimize leakage, while in [18], [19], and [20], the surrounding flux is essential for 2-D/3-D power transfer, but it could not be controlled or shaped at a particular position. Shielding would be a big concern in such systems considering multi-Rx charging applications. Leaving aside the

**TABLE 1. Comparison Between the Proposed System and Other Multi-Rx WPT Systems**

Reference and structure		Number of converters and tuning circuits	Core material of coils	Magnetic leakage reduction	Charging freedom	Full positional freedom in the charging area for	
						Single Rx	Multi-Rx
Single Tx	[20]: 2D WPT	1	ferrite	×	2D	×	
	[20]: 3D WPT	1	air	×	3D	×	
	[19]	1	air	×	2D	✓ naturally uniform magnetic field	
Multi-Tx	[21]: with $n$ TxS	$n$	ferrite	need dynamic ON/OFF control	2D	need active phase control + amplitude regulation	×
	[14], [15], [18]	3	air	×	3D	need active phase control	×
	proposed	1	air	✓	2D	✓ naturally uniform magnetic field	

total area to be shielded, it should not narrow down the power transfer freedom, but then magnetic leakage easily happens in those areas where an Rx is not presented. In comparison, the proposed structure confines most of the magnetic flux inside the valid charging space (the 2-D torus) with proper design. All the “useful” flux is captured and confined inside the Rx charging space, so the leakage is greatly reduced. The poloidal flux leakage of the design can be easily minimized by adding two shielding boards on top and bottom of the structure with a small size.

The rest of this article is organized as follows. In Section II-A, we introduce the proposed WPT link structure and provide an analysis on the field distribution. An equivalent circuit for the WPT system is presented in Section III, together with detailed equations describing the system operations based on both the ideal and realistic (including parasitics) models. Also, the design accuracy regarding parasitic effects is discussed. In Section IV, parasitic effects are analyzed in detail considering the system output performance and efficiency. Tolerances for parasitic parameters are as a supplement for the WPT link design. The experimental results in Section V validate the working principles of the proposed coil structure. Finally, Section VI concludes this article.

## II. COIL STRUCTURE AND MAGNETIC FIELDS

### A. PROPOSED COIL STRUCTURE

In this section, we introduce and explain the proposed geometry of the WPT coils. The proposed WPT system consists of coils of three types, including a helical transmitter coil (Tx), spiral-shaped receiver coils (Rxs), and a repeater coil (Rp), as illustrated in Fig. 1. The Tx coil is connected to a high-frequency ac voltage source. The repeater coil that comprises two types of coils connected in series, is designed to be coupled with both the Tx coil and Rx coils. First, an inner helical coil is positioned at the center of the repeater to generate a poloidal field that strongly couples with the Tx coil. Second, a toroidal coil is wound along the torus, creating a conformal toroidal field flowing inside the torus. As a result, the repeater generates both the poloidal and toroidal fields, enabling the coaxial placement of the Tx coil with the inner coil of the repeater, and Rx coils can be inserted into each turn slot of the toroidal coil of the repeater. With this arrangement,

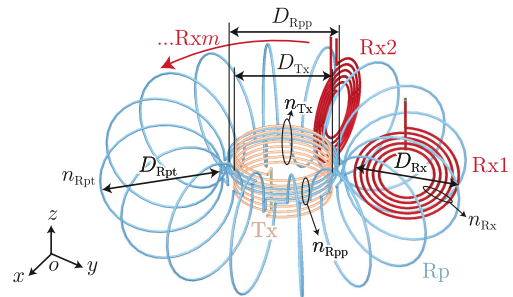


**FIGURE 1. Illustration of the proposed coil geometry.**

we achieve a strong coupling between the Tx and Rp coils as well as Rp and Rx coils, while having negligible direct coupling between the Tx and Rx coils.

The size parameters of the coils are shown in Fig. 1, where  $n_{...}$  represent the numbers of turns, and  $D_{...}$  are the diameters of coils. The subscripts Tx and Rx denote the transmitter or receiver coils, respectively. The subscripts Rpp and Rpt indicate the poloidal and toroidal parts of the repeater coil, respectively. All the size parameters can be adjusted flexibly according to the application specifications or limitations on parasitic effects, which will be discussed in detail in the following. For instance, the number of turns of the Tx coil ( $n_{Tx}$ ) and the poloidal part of the repeater ( $n_{Rpp}$ ) can be varied to achieve the desired mutual inductance between Tx and Rp coils. Similarly, the diameter of the toroidal turn of the repeater ( $D_{Rpt}$ ) can be modified to ensure the desired mutual inductance between Rp and Rx coils to collect most of the toroidal flux of the repeater. However, it is noticeable that parasitic effects, including the parasitic resistances of the coils, intrinsic capacitances, and undesired cross-couplings, would degrade the system performance at the high operating frequency of 6.78 MHz [13], [28]. The effects of parasitic parameters on system operations will be discussed in Section III-B.

Next, we study the field distributions and how they are related to the dimensions of the repeater coil to get an insightful understanding of the field interactions and determine the optimal structure of the proposed coils.

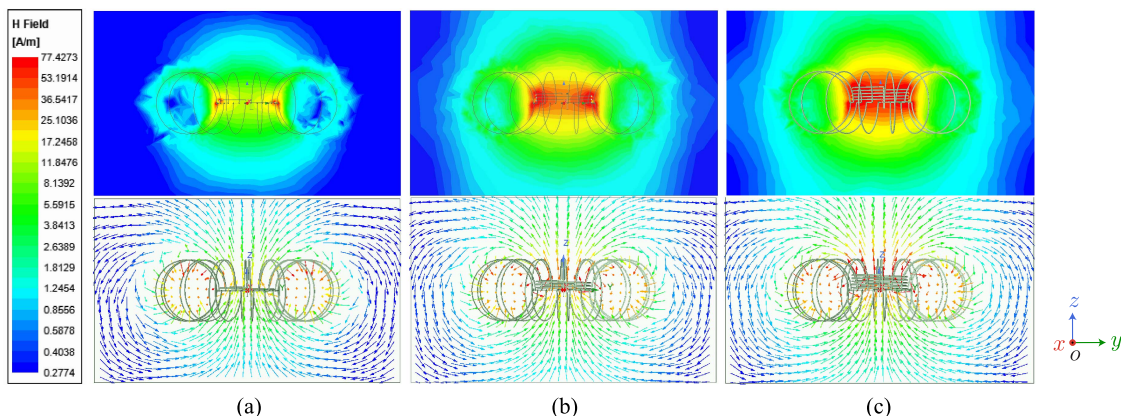


**FIGURE 2.** Magnetic field magnitude (in the  $yoz$ -plane) and front-view vector plots for the poloidal field with a varying number of repeater turns (a)  $n_{Rpp} = 2$ , (b)  $n_{Rpp} = 4$ , and (c)  $n_{Rpp} = 6$ . The Tx number of turns is fixed at  $n_{Tx} = 6$ , and the other dimensional parameters are given in Table 2.

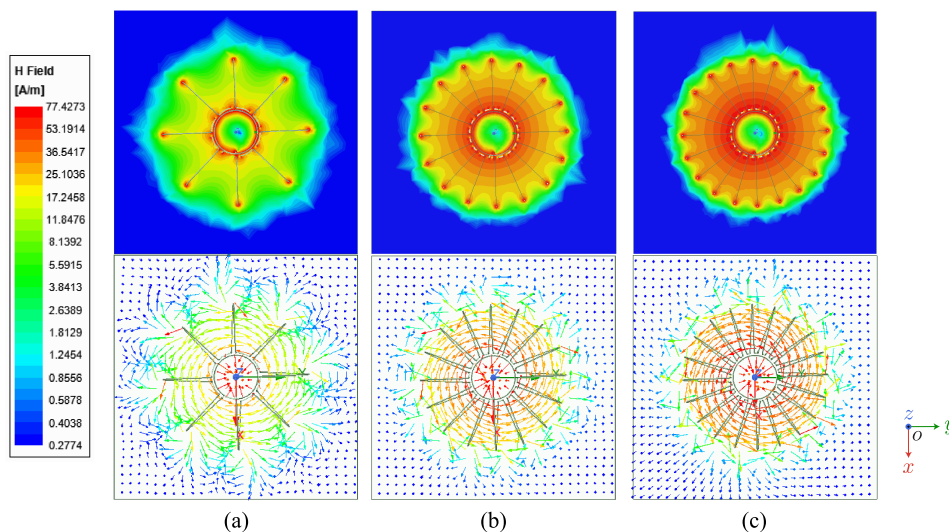


**FIGURE 3.** Simulated magnetic field magnitude (in the  $xoy$ -plane) and top-view vector plots for rotating toroidal field with a varying number of toroidal turns (a)  $n_{Rpt} = 8$ , (b)  $n_{Rpt} = 16$ , and (c)  $n_{Rpt} = 20$ . The other dimensional parameters follow Table 2.

## B. POLOIDAL FIELD ANALYSIS

The inner poloidal section of the repeater exhibits significant coupling with the helical Tx coil, which is positioned as coaxial turns within the repeater. The mutual inductance between Tx and Rp depends on the number of turns in the Tx coil ( $n_{Tx}$ ) and the number of turns in the poloidal winding of the Rp coil ( $n_{Rpp}$ ). The poloidal fields generated by the repeater coil with varying numbers of turns are illustrated in Fig. 2. Fig. 2(a) depicts the magnetic field with two poloidal turns, where the center area of the repeater exhibits a considerably weak field. However, as shown in Fig. 2(b) and (c), the poloidal fields improve significantly when the number of turns is increased to four and six, respectively. Increasing the number of poloidal turns not only improves the poloidal fields but also lengthens the repeater, causing some nonuniformity in the current distribution and increasing parasitic resistance. To balance these factors, a reasonable choice in this example is four poloidal turns. The Tx–Rp coupling can be compensated by increasing the number of turns of the Tx coil.

## C. TOROIDAL FIELD ANALYSIS

Next, we explore the influence of the number of toroidal turns ( $n_{Rpt}$ ) of the repeater on the rotating toroidal field. Fig. 3 presents a top view of the coil, showcasing the toroidal field distributions for different numbers of turns. The toroidal field flows parallel to the  $xoy$ -plane. As illustrated in Fig. 3(a), using 8 toroidal turns generates a moderate magnitude of the toroidal field with the toroidal vectors rotating inside the turns. However, the field spreads outside the torus, leading to undesirable leakage flux that could interfere with foreign objects. It is apparent that the toroidal turns in this example are not sufficiently dense to confine the field within the torus. Hence, we increase the number of toroidal turns to 16 and 20, as depicted in Fig. 3(b) and (c), respectively. In both cases, the toroidal field is significantly improved and effectively confined inside the torus compared to the 8-turn case, resulting in a substantial reduction of the leakage flux in the vicinity of the coil. However, there is no notable change in the magnitude of the field between these two cases. Considering the overall length of the

**TABLE 2. Dimensions of the Coils**

		diameter $D$ (cm)		number of turns $n$	
Tx	poloidal	$D_{Tx}$	9.4	$n_{Tx}$	6
Rp	poloidal	$D_{Rpp}$	10	$n_{Rpp}$	4
	toroidal	$D_{Rpt}$	10	$n_{Rpt}$	16
Rx	toroidal	$D_{Rx}$	10	$n_{Rx}$	8

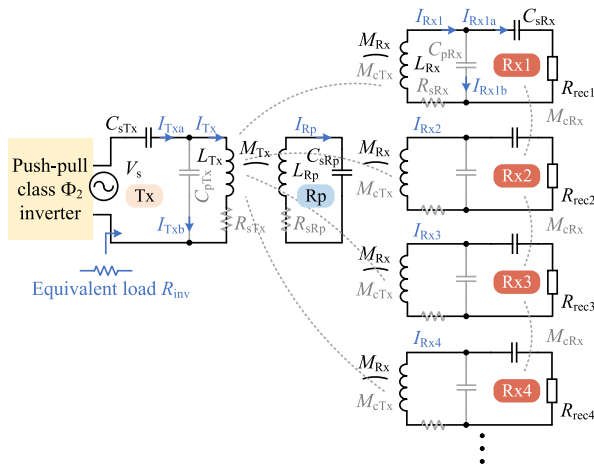


**FIGURE 4. Equivalent circuit of the proposed multi-Rx WPT system.**

repeater,  $n_{Rpt} = 16$  can be chosen to prevent nonuniformity of the current distribution and increased parasitic resistance in the repeater coil. Moreover, the mutual inductance between the Rp and the Rx coil can further be enhanced by optimizing the number of turns.

Therefore, we choose a repeater configuration consisting of four poloidal turns and 16 toroidal turns. The diameters of the coils are chosen according to a portable and mobile device application, however, they can be easily modified to suit other applications. The dimensions of the coils in the WPT link are summarized in Table 2.

The presented results of simulations as well as discussions in this section provide insight on setting the lower limit on the number of turns, considering the field density requirement (related to  $\eta_{WPT}$ ), while the requirements on the total length and the level of parasitic effects help us to set the upper limit on the number of turns. The upper boundaries for the number of turns as well as the parasitic parameters will be discussed in the next two sections, based on the analysis of design accuracy, the load-independence requirement, and the target on high efficiency.

### III. THEORETICAL ANALYSIS OF THE SYSTEM

First, we analyze the working principles of the proposed WPT system under both the ideal and realistic (including parasitics) conditions. The equivalent circuit model of the proposed multi-receiver WPT system is depicted in Fig. 4, where a push-pull T-network (PPT) class- $\Phi_2$  converter is used to supply a constant voltage (CV) to the Tx coil, and passive rectifiers are

connected to the Rx coils for ac–dc conversion. The class- $\Phi$  resonant converter can be easily designed for system specifications based on the parameter design steps in [29]. The WPT stage contains a transmitter, a repeater, and several receivers (the total number of Rx's represented as  $m$ ), where each coil is tuned to the working frequency  $f_s = 6.78$  MHz with a series capacitor  $C_{scoil}$  (subscript  $coil$  can be Tx, Rp, or Rx). The mutual inductance between Tx and Rp is modeled as  $M_{Tx}$ , and  $M_{Rxxk}$  represents the mutual inductance between the Rp and the  $k^{th}$  Rx coil,  $k = 1, 2, \dots, m$ . In the following, we always consider identical spiral-type Rx coils and the uniformly distributed toroidal flux in Fig. 3, thus, assume that all the Rp-Rx mutual inductances have the same value, i.e.,  $M_{Rxxk} = M_{Rx}$ .

As an example of multiple receivers, four Rx devices are shown in Fig. 4, while the number of receivers,  $m$ , in this WPT system can be modified according to the application requirements. The ideal case model without parasitic parameters is drawn in black, and three types of coil parasitic components are indicated in gray color, including

- 1) parasitic resistance  $R_s$ , represented by the quality factors  $Q_{coil} = \omega_s L_{coil} / R_{scoil}$  (subscript  $coil$  can be Tx, Rp, or Rx);
- 2) cross-coupling mutual inductance
  - a) between the Tx coil and an Rx coil  $M_{cTx}$ , represented by the cross-coupling ratio  $\gamma_t = M_{cTx} / M_{Rx}$ ;
  - b) between two adjacent Rx coils  $M_{cRx}$ , represented by the cross-coupling ratio  $\gamma_r = M_{cRx} / M_{Rx}$ ;
- 3) parallel capacitance  $C_{pcoil}$ , represented by the self-resonance frequency of the coils  $f_{rcoil} = 1 / (2\pi \sqrt{C_{pcoil} L_{coil}})$ .

It is noted that in the proposed structure, the stray capacitance between turns from different coils, i.e., Tx and Rp, can be easily minimized without sacrifice of any performance by creating a gap between these turns, cf. a difference in the coil diameter  $D_{Tx}$  and  $D_{Rpp}$  in Table 2. Therefore, the parasitic effect of mutual capacitance is not considered in this article. In the model that includes parasitic components, the currents flowing through the Tx and Rx coil inductors, i.e.,  $L_{Tx}$  and  $L_{Rx}$ , are represented by  $I_{Tx}$  and  $I_{Rx}$ , respectively.  $I_{Txka}$  (or  $I_{Rxka}$ ) and  $I_{Txkb}$  (or  $I_{Rxkb}$ ) represent the current flowing through the series-compensation capacitor  $C_{scoil}$  and the parallel parasitic capacitor  $C_{pcoil}$  of  $L_{Tx}$  (or  $L_{Rx}$ ). Since the repeater loop in Fig. 4 contains only the Rp coil inductance  $L_{Rp}$ , its parasitic capacitance  $C_{pRp}$ , and the compensation capacitor  $C_{sRp}$ , the two capacitors can be seen as equivalent to a single one. The current flowing through the repeater loop is labeled as  $I_{Rp}$ .  $R_{rec} = R_{reck}$  represents the equivalent load connected in series with the  $Rx_k$  coil and its compensation capacitor  $C_{sRx}$ , which includes the passive rectifier circuit with a dc load resistor.

System modeling accounting for these parasitic effects will be discussed in detail in Section III-B.

#### A. SYSTEM MODELING FOR IDEAL-CASE SCENARIOS AND WITH PARASITICS

In the ideal case, the coils are assumed to be purely inductive, and their self-resonance frequencies  $f_r$  are considered to be

infinitely high. The coils are assumed to be lossless with  $Q_{coil} \rightarrow \infty$  and  $R_{scoil} = 0$ . A series compensation capacitor is applied to each coil, tuning the  $LC$  branch to resonance at  $f_s$ . The PPT class- $\Phi_2$  inverter is connected to the Tx input, supplying a constant sinusoidal voltage with the amplitude  $V_s$ .

There is no cross-coupling in the ideal-case system, meaning that the mutual inductance between Tx and Rx coils ( $M_{cTx}$ ) and the mutual inductance between two Rx coils ( $M_{cRx}$ ) are assumed to be zero. By applying the Kirchhoff's circuit law to the Tx, Rp, and Rx loops in Fig. 4, the amplitude of current flowing through each coil in the ideal case is written as

$$\vec{I}_{Tx(I)} = \left( \frac{M_{Rx}}{M_{Tx}} \right)^2 \frac{\vec{V}_s}{R_{rec}} \quad (1)$$

$$\vec{I}_{Rp(I)} = -j \frac{\vec{V}_s}{\omega_s M_{Tx}} \quad (2)$$

$$\vec{I}_{Rx(I)} = -\frac{M_{Rx}}{M_{Tx}} \frac{\vec{V}_s}{R_{rec}} \quad (3)$$

where  $\vec{I}_{Tx(I)}$ ,  $\vec{I}_{Rp(I)}$ , and  $\vec{I}_{Rx(I)}$  are the vectors of currents flowing through the transmitter, the repeater, and the receiver inductors. It is evident from (2) that the repeater coil in this WPT system acts as a constant current (CC) source, which works independently from the load resistance. According to (3), the output voltage of each Rx is expressed as

$$\vec{V}_{rec(I)} = \vec{I}_{Rx(I)} R_{rec} = -\frac{M_{Rx}}{M_{Tx}} \vec{V}_s \quad (4)$$

so we obtain a load-independent CV at the output of each receiver. With  $m$  Rxs presented in the system, the input impedance of the WPT link, seen at the inverter output,  $Z_{inv}$  is calculated as

$$Z_{inv} = R_{inv} = \frac{V_s}{I_{Tx}} = \frac{1}{m} \frac{M_{Tx}^2}{M_{Rx}^2} R_{rec} \quad (5)$$

which is equivalent as having  $m$  parallel-connected impedances, each of them reflected from a single Rx.

## B. MODELING ACCURACY CONSIDERING PARASITIC EFFECTS AT MULTI-MHZ FREQUENCIES

In high-frequency systems, parasitic effects become more significant, and the ideal-case equations do not model the system enough accurately. In this subsection, we discuss the system operation by incorporating all the three types of parasitic effects defined at the beginning of Section III.

The system is analyzed with an example WPT system with  $m$  receiver loads. Each type of parasitic effects is individually analyzed to understand their impact on the system output features, i.e., the repeater current  $I_{Rp}$  and the Rx output voltage  $V_{rec}$ . Corresponding analytical equations for currents and voltages are given. Subsequently, numerical investigations are conducted using the coil specifications outlined in Table 2 to illustrate the impact of individual parasitic effects on system modeling. Following that, the actual system outputs  $I_{Rp}$  and  $V_{rec}$  are calculated by considering all three types of

parasitic parameters together. To differentiate the current or voltage components through separate parasitic analysis from the ideal cases (with an extra subscript  $(I)$ ) or joint-case analysis (without extra subscript), we define three extra subscripts to represent these three types of parasitic effects. The nominal current or voltage

- 1) considering the parasitic resistance effect is represented by an extra subscript  $(r)$ , e.g., the Rp current considering  $R_s$  effect is  $I_{Rp(r)}$ ;
- 2) considering the cross-coupling effects is represented by an extra subscript  $(c)$ , e.g., the Rp current considering  $M_{cTx}$  or  $M_{cRx}$  effect is  $I_{Rp(c)}$ ;
- 3) considering the parasitic capacitance effect is represented by an extra subscript  $(f)$ , e.g., the Rx output voltage considering  $f_r$  effect is  $V_{rec(f)}$ .

Compared to the values in the actual system, a tolerance of  $\pm 10\%$  on the load voltage or Rp current is generally accepted. We will separately compare the accuracy of the ideal-case modeling equations and the equations with each parasitic effect, and find the boundaries for each parasitic parameter values where the parasitic-case equations can model the system with high accuracy (i.e., with  $< 10\%$  variation).

### 1) COIL PARASITIC RESISTANCE $R_s$

By considering only the parasitic resistances  $R_{sTx}$ ,  $R_{sRp}$ , and  $R_{sRx}$ , while assuming  $f_r \rightarrow \infty$ ,  $M_{cTx} = M_{cRx} = 0$ , the current and voltage components in the WPT coils are obtained as

$$I_{Tx(r)} = \frac{[R_{sRp}(R_{rec} + R_{sRx}) + m(\omega_s M_{Rx})^2] V_s}{H1} \quad (6)$$

$$I_{Rp(r)} = \frac{-j\omega_s M_{Tx}(R_{rec} + R_{sRx}) V_s}{H1} \quad (7)$$

$$V_{rec(r)} = \frac{\omega_s^2 M_{Tx} M_{Rx} R_{rec} V_s}{H1} \quad (8)$$

where  $H1 = \omega_s^2 [m M_{Rx}^2 R_{sTx} + M_{Tx}^2 (R_{rec} + R_{sRx})] + R_{sTx} R_{sRp} (R_{rec} + R_{sRx})$ . When the quality factors of all the coils are high enough, the parasitic resistance is negligibly small and (6)–(8) are simplified to (1), (2), and (4).

With regard to different quality factor values for three coils  $Q_{Tx}$ ,  $Q_{Rp}$ , and  $Q_{Rx}$ , Fig. 5(a) and (d) show the output characteristics, i.e., the Rp current and Rx voltage, calculated using the ideal-case equations [cf.  $I_{Rp(I)}$ ,  $V_{rec(I)}$  from (1)–(4)] and from the  $R_s$ -parasitic equations [cf.  $I_{Rp(r)}$ ,  $V_{rec(r)}$  in (6)–(8)] as the ratios compared to their real-case values with all the parasitics considered,  $I_{Rp}$  and  $V_{rec}$ , from the joint numerical calculation. As an example, the results for  $Q_{Tx}$  variation are calculated with  $Q_{Rp} = 100$ ,  $Q_{Rx} = 400$ , and  $I_{Rp}$  and  $V_{rec}$  are calculated based on the other parasitics with  $f_r = 5f_s$ ,  $\gamma_t = 0$ ,  $\gamma_r = 0.07$ . Performance evaluation for  $Q_{Rp}$  and  $Q_{Rx}$  variations is done in a similar manner [see the notes given in Fig. 5(a)].

Numerical calculations demonstrate that regardless of the quality factor values in each coil, the  $R_s$ -parasitic equations accurately model the practical system, showing a good agreement with the real case within a deviation range  $-5\%$  to

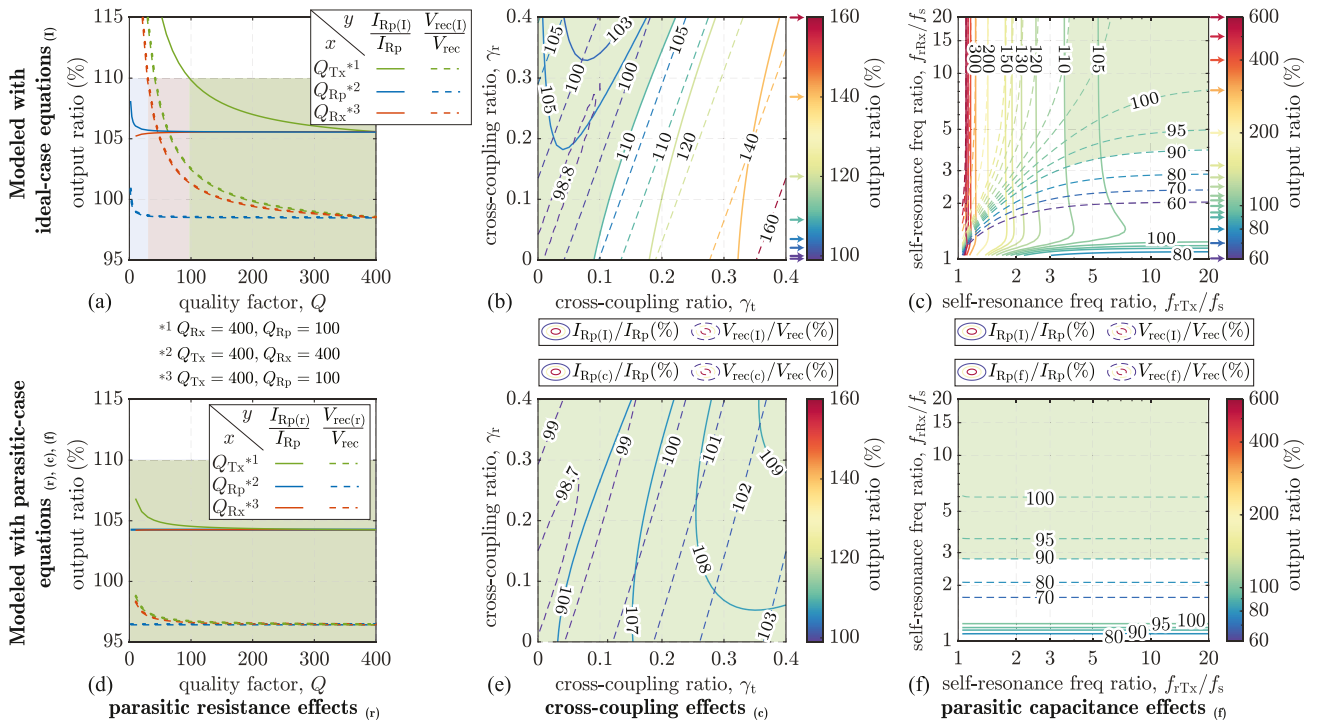


**FIGURE 5.** WPT link output ratio (%) (a)–(c) calculated with the *ideal-case (1)–(4)*, and (d)–(f) calculated using the *equations including parasitic effects (7)–(15)*, normalized to the *real-case results under joint numerical analysis with all three types of parasitics*. Analysis in terms of: (a),(d) parasitic resistance effect ( $f_r = 5f_s, \gamma_t = 0, \gamma_r = 0.07$ ):  $\frac{I_{Rp(r)}}{I_{Rp}}$  and  $\frac{V_{rec(r)}}{V_{rec}}$  with regard to the quality factors  $Q_{Tx}, Q_{Rp}$ , and  $Q_{Rx}$  variations. (b),(e) cross-coupling effect ( $f_r = 5f_s, Q_{Tx} = Q_{Rx} = 330, Q_{Rp} = 100$ ):  $\frac{I_{Rp(c)}}{I_{Rp}}$  and  $\frac{V_{rec(c)}}{V_{rec}}$  with regard to the cross-coupling ratio  $\gamma_t$  and  $\gamma_r$  variations. (c),(f) parasitic capacitance effect ( $Q_{Tx} = Q_{Rx} = 330, Q_{Rp} = 100, \gamma_t = 0.02, \gamma_r = 0.1$ ):  $\frac{I_{Rp(f)}}{I_{Rp}}$  and  $\frac{V_{rec(f)}}{V_{rec}}$  with regard to the self-resonance frequency ratio  $\frac{f_{rTx}}{f_s}$  and  $\frac{f_{rRx}}{f_s}$  variations.

+10%. However, the modeling accuracy with the ideal-case equations deteriorates when  $Q$  is low, especially for the Tx coil. For the example WPT system, the ideal-case equations (1)–(4) are valid only for coils with  $Q_{Tx} > 100, Q_{Rp} > 2, Q_{Rx} > 40$ .

## 2) CROSS-COUPLING BETWEEN TX–RX OR RX–RX

Similarly, predominantly considering the cross-couplings between Tx and Rxs ( $M_{cTx}$ ) and between Rxs ( $M_{cRx}$ ), the currents and the output voltage are calculated as

$$I_{Tx(c)} = \frac{mM_{Rx}^2 V_s}{M_{Tx}H2} \quad (9)$$

$$I_{Rp(c)} = \frac{(-jM_{Tx}R_{rec} + 2\omega_s M_{Rx} [\gamma_r M_{Tx} - 2\gamma_t M_{Rx}]) V_s}{\omega_s M_{Tx}H2} \quad (10)$$

$$V_{rec(c)} = \frac{-M_{Rx}R_{rec}V_s}{H2} \quad (11)$$

where  $H2 = M_{Tx}R_{rec} + j2\omega_s M_{Rx}(\gamma_r M_{Tx} - m\gamma_t M_{Rx})$ , and  $\gamma_t$  and  $\gamma_r$  are the cross-coupling coefficients. Considering variations of both Tx–Rx and Rx–Rx cross-couplings  $\gamma_t, \gamma_r \in [0, 0.4]$ , the load resistance  $R_{rec}$  is included in the  $I_{Rp(c)}$  and  $V_{rec(c)}$  equations. To maintain load-independent operations, the relation between  $\gamma_t$  and  $\gamma_r$  needs to be carefully designed.

We will discuss the region for maintaining load-independence in Section IV-A.

Fig. 5(e) shows the Rp current  $I_{Rp(c)}$  and the Rx output voltage  $V_{rec(c)}$  calculated from (9)–(11) normalized to their real-case values. Within the given range for  $\gamma_t$  and  $\gamma_r$ , the  $M_c$ -equations always give  $I_{Rp(c)}$  and  $V_{rec(c)}$  results with above 90% accuracy. In comparison, as seen in Fig. 5(b), the ideal-case equations may easily give a value of  $V_{rec(l)}$  60% higher than the real-case one. To maintain the same accuracy level above 90%, as in Fig. 5(e), the validity range for the ideal-case equations shrinks to the green-shaded area.

## 3) COIL PARASITIC CAPACITANCE $C_p$

The parasitic capacitance of coils is modeled by their self-resonance frequency  $f_r$  (or the angular frequency  $\omega_r = 2\pi f_r$ ). Since the repeater loop in Fig. 4 does not contain any source or load, the self-resonance of Rp coil will not lead to any negative effect on the system as long as  $f_{rRp} > f_s$ , and the Rp coil is tuned properly to the operating frequency  $f_s$ . Since only the parallel capacitances of Tx and Rx can have a detrimental effect, the self-resonance frequencies of Tx and Rx are taken into consideration for the analysis. When the other parasitic effects are considered negligibly small, the current and voltage

equations are derived as

$$\Re [I_{T_x(f)}] = \frac{4M_{R_x}^2 \omega_{rR_x}^4 (\omega_{rT_x}^2 - \omega_s^2)^2}{M_{T_x}^2 \omega_{rT_x}^4 (\omega_{rR_x}^2 - \omega_s^2)^2} \frac{V_s}{R_{rec}} \quad (12)$$

$$\tan \phi_{(f)} = \left(1 - \frac{\omega_s^2}{\omega_{rR_x}^2}\right) \frac{\omega_s^2}{\omega_{rR_x}^2} \frac{R_{rec}}{\omega_s L_{R_x}} + \left(1 - \frac{\omega_s^2}{\omega_{rR_x}^2}\right)^2 \frac{\omega_s^2}{\omega_{rT_x}^2 - \omega_s^2} \frac{M_{T_x}^2}{4M_{R_x}^2} \frac{R_{rec}}{\omega_s L_{T_x}} \quad (13)$$

$$I_{Rp(f)} = -j \frac{V_s}{\omega_s M_{T_x}} \left(1 - \frac{\omega_s^2}{\omega_{rT_x}^2}\right) \quad (14)$$

$$V_{rec(f)} = -\frac{M_{R_x} V_s \omega_{rR_x}^2 (\omega_{rT_x}^2 - \omega_s^2)}{M_{T_x} \omega_{rT_x}^2 (\omega_{rR_x}^2 - \omega_s^2)} \quad (15)$$

Equations (14) and (15) show that although the presence of a parasitic capacitance alters the repeater current and the load voltage, these variables remain load-independent. Therefore, apart from the mutual inductance ratio, it is feasible to design the voltage gain through an  $f_r$  adjustment, e.g., realize a higher voltage gain with the same mutual inductance. However, considering the other two types of parasitic effects exist in the system, a very low  $f_r$  comparable to  $f_s$  might destroy the load-independent operations. Therefore, a boundary should still be set for  $f_{rT_x}$  and  $f_{rR_x}$  to ensure load-independent  $V_{rec}$  and  $I_{Rp}$ , which will be discussed in detail in Section IV-A. Besides, the phase of the Tx current is not load-independent, as is seen from (12) to (13). With a low  $\omega_{rT_x}$  or  $\omega_{rR_x}$  self-resonance frequencies, the Tx supply current experiences a significant phase shift during load variations. This can have detrimental effects on both efficiency and the inverter soft-switching operations.

On the other hand, considering the modeling accuracy, the conventional ideal-case equations cannot model the  $C_p$  effect on voltage gain. As seen from Fig. 5(c), (1)–(4) are valid only for high  $f_r$ , when their effects on the voltage gain are negligibly small. To have a better accuracy of the system modeling and take advantage of  $C_p$  effects on voltage gain design, the  $C_p$ -parasitic equations need to be used, which provide more than 90% accuracy compared to the practical case, see Fig. 5(f).

In summary, the analysis in this section involved examinations of the WPT system operations both in the ideal case and when including parasitic effects. The ideal-case equations impose very strict requirements on the parasitic parameters to ensure good design accuracy. In contrast, equations that account for three types of parasitic effects separately maintain good accuracy with the tolerance of even high parasitic parameter values. Equations (6)–(15) are always valid with a higher accuracy as long as the Rx self-resonance frequency  $f_{rR_x} > 2.8f_s$ , comparing to the ideal-case (1)–(4).

#### IV. DESIGN PROCEDURE

In this section, we analyze parasitic effects on system output characteristics including load-independence and WPT

link efficiency. We provide guidance for designing the proposed WPT systems by establishing the upper boundaries for all parasitic parameters. Combining with the analysis in Sections II-A and III-B, we can determine overall boundaries for parasitic parameters as well as for the WPT link dimensions.

The numerical values of the Rp current and the Rx output voltage influenced by parasitic effects of all three types are analyzed. Based on an assumed  $\pm 5\%$  tolerance on the load-independent output characteristics, boundaries for each parasitic parameter are established. This comprehensive analysis facilitates an informed and optimized design process, ensuring the desired performance and efficiency of the proposed WPT system.

#### A. LOAD-INDEPENDENCE DISCUSSION REGARDING PARASITIC EFFECTS

Fig. 6 presents the Rp current and Rx output voltage at 10%-load normalized to their values at full-load which are obtained through numerical calculation with all the parasitic effects considered.

##### 1) COIL PARASITIC RESISTANCE $R_s$ EFFECT

Considering all the parasitic parameters  $f_r = 5f_s$ ,  $\gamma_t = 0$ ,  $\gamma_r = 0.07$ , the current and voltage at 10%-loaded situation are given in Fig. 6(a) with regard to variations of  $Q_{T_x}$ ,  $Q_{R_p}$ , and  $Q_{R_x}$  individually. Both  $I_{Rp(0)}$  and  $V_{rec(0)}$  are normalized to their corresponding full-loaded values to facilitate straightforward comparison.

The green curve in Fig. 6(a) represents the impact of varying  $Q_{T_x}$  while keeping  $Q_{R_p} = 100$ ,  $Q_{R_x} = 400$ . It demonstrates that the quality factor of the Tx coil has a significant effect on load-independence of both  $I_{Rp}$  and  $V_{rec}$ . To ensure that the load-dependence of  $V_{rec}$  stays within a 5% variation, a minimum  $Q_{T_x}$  value of 150 is recommended. On the other hand, the value of  $Q_{R_p}$  does not have a significant impact on the load-independence of both  $V_{rec}$  and  $I_{Rp}$ , as is seen from the blue curves in Fig. 6(a). The 10%-load voltage  $V_{rec(0)} = 102\%V_{rec}$  comes from the effects from nonideal  $Q_{T_x}$  and  $Q_{R_x}$ . Finally, the influence of  $Q_{R_x}$  is primarily observed in the Rx output, as seen from the red lines in Fig. 6(a). To keep the load-independence tolerance within  $\pm 5\%$  (i.e.,  $V_{rec(0)}/V_{rec} < 105\%$ ), we set the boundary of the Rx quality factor as  $Q_{R_x} > 110$ .

##### 2) CROSS-COUPLING BETWEEN TX–RX OR RX–RX

To analyze the load-independence with different cross-coupling levels between Tx–Rx or Rx–Rx, we consider a scenario with predefined quality factors and self-resonance frequencies of each coil, which are selected within the boundary set in the above sections, e.g.,  $Q_{T_x} = Q_{R_x} = 330$ ,  $Q_{R_p} = 100$ ,  $f_{rT_x} = f_{rR_x} = 5f_s$ . In Fig. 6(b), the Tx–Rx cross-coupling ratio  $\gamma_t$  and Rx–Rx cross-coupling ratio  $\gamma_r$  are varied as  $x$  and  $y$  coordinates, respectively. The contour plot represents the 10%-load to full-load ratio of the Rp current and Rx voltage,  $I_{Rp(0)}/I_{Rp}$  and  $V_{rec(0)}/V_{rec}$ .



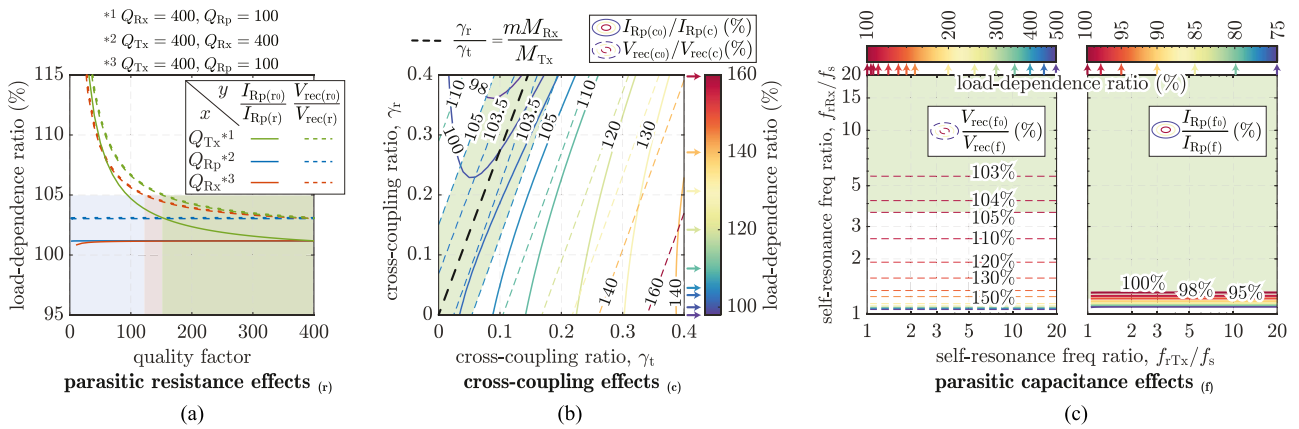


**FIGURE 6.** Rp current and Rx output voltage at 10%-load,  $I_{Rp(r,c,f_0)}$  and  $V_{rec(r,c,f_0)}$ , normalized to the full-load values  $I_{Rp}$  and  $V_{rec}$ . (a) With varied quality factors  $Q_{Tx}$ ,  $Q_{Rp}$ ,  $Q_{Rx} \in [2, 400]$  (when  $f_r = 5f_s$ ,  $\gamma_t = 0$ ,  $\gamma_r = 0.07$ ). (b) With varied cross-coupling coefficients  $\gamma_t$ ,  $\gamma_r \in [0, 0.4]$  (when  $f_r = 5f_s$ ,  $Q_{Tx} = Q_{Rx} = 330$ ,  $Q_{Rp} = 100$ ). (c) With varied self-resonance frequencies  $f_{rTx}$ ,  $f_{rRx} \in [1.05, 20]f_s$  (when  $Q_{Tx} = Q_{Rx} = 330$ ,  $Q_{Rp} = 100$ ,  $\gamma_t = 0.02$ ,  $\gamma_r = 0.1$ ).

Considering the Rp current, load-independent characteristics can be achieved by designing the cross-coupling ratios  $\gamma_t$  and  $\gamma_r$  according to the 100 %-labeled curve in Fig. 6(b). However, achieving load-independent Rp current (i.e.,  $I_{Rp(0)} = I_{Rp}$ ) does not guarantee load-independence of the output voltage. Equation (11) shows that the Tx–Rx and Rx–Rx cross-coupling effects cancel each other when the cross-coupling ratios are related as

$$\gamma_t M_{Tx} - m\gamma_r M_{Rx} = 0. \quad (16)$$

The dashed-line curve in Fig. 6(b) also reveals a similar trend. The shaded area represents the 5 % variation of the output voltage  $V_{rec(0)}$ . By satisfying (16) for cross-coupling ratios, the minimum variation of the output voltage from full load to 10 % load is achieved within the shaded area. It should be noted that values  $V_{rec(0)}/V_{rec} > 100\%$  come due to effects of the other parasitics. Therefore, in order to obtain load-independence in system output voltage, it is recommended to design the cross-coupling ratio around the relation given by (16). However, accurately controlling cross-coupling in design process can be challenging. This relation can be used to tune the system by adjusting the coil structures.

### 3) COIL PARASITIC CAPACITANCE $C_p$

Next, moving forward to the discussion on the effects of the coil parasitic capacitance, we analyze this effect in terms of the self-resonance frequency. In Fig. 6(c), the Rp current and Rx voltage at 10 %-load normalized to the full-load values are plotted for different self-resonance frequencies of the Tx and Rx coils. Although a low self-resonance frequency of Rx provides a higher voltage gain in the WPT link, see (15), it is seen in Fig. 6(c) that the system loses its load-independent voltage output property at low  $f_{rRx}$  values. In contrast, the load-independent characteristic of the Rp current is almost not affected by low  $f_{rRx}$ .

Therefore, to maintain the load-independent output voltage with a 5 % tolerance, it is suggested that the self-resonance

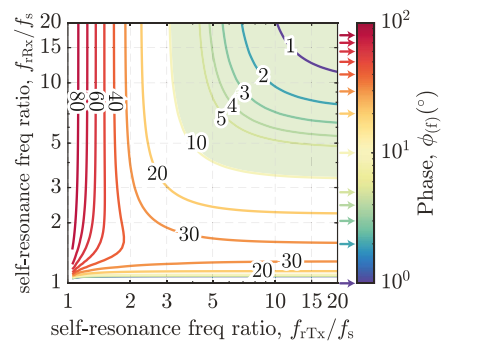


**FIGURE 7.** Phase difference  $\phi$  between Tx input current and voltage.

frequency of Rx should be higher than  $3.5f_s$ . On the other hand, the Tx coil self-resonance frequency appears to be neither limited by design accuracy nor the load-independence requirement. However, the power factor angle for the inverter output as well as the WPT link efficiency will set the limit on  $f_{rRx}$ , the later one will be discussed in the next subsection.

To obtain an equivalent resistive load at the inverter output, when the inverter output current and voltage are in phase, i.e.,  $\cos \phi = 1$ , the WPT stage is tuned to resonance at the operating frequency  $f_s$  at full load. Fig. 7 shows  $\phi(0)$ , the inverter output phase angle at the 10 % load, with regard to different self-resonance frequencies of Tx and Rx coils. A positive  $\phi(0)$  represents an inductive load (i.e., lagging current) for the inverter. Therefore, although the Tx current and voltage are tuned to be in-phase at full load, the phase difference is a load-dependent variable, and the dependency is affected by  $f_{rTx}$  and  $f_{rRx}$ . A large phase deviation may lead to a negative effect on the inverter operations, destroy the soft-switching conditions and lower the efficiency. Considering the relation between the active power and apparent power, a large  $\phi(0)$  also leads to a lower power factor, which reduces the WPT link efficiency as compared to low- $\phi(0)$  systems with the same power levels.

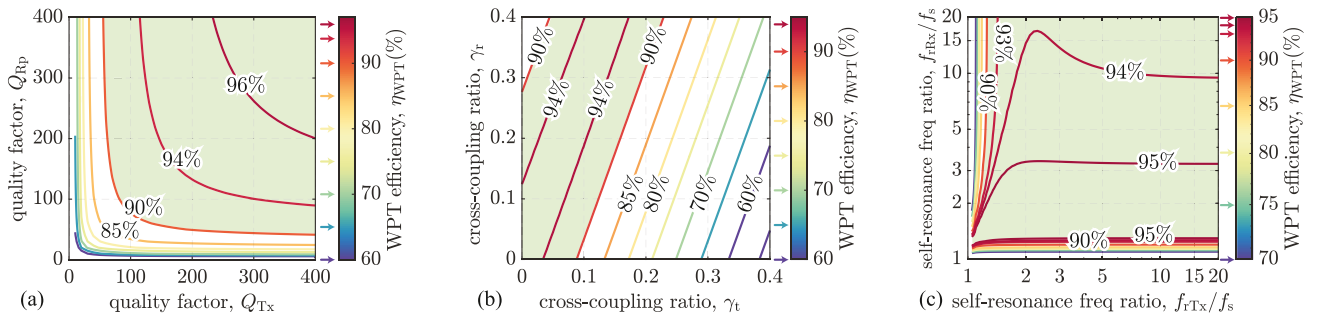


**FIGURE 8.** WPT link efficiency  $\eta_{\text{WPT}}$ . (a) With varied quality factors  $Q_{\text{Tx}}$ ,  $Q_{\text{Rp}}$ ,  $Q_{\text{Rx}} \in [2, 400]$  (when  $f_r = 5f_s$ ,  $\gamma_t = 0$ ,  $\gamma_r = 0.07$ ). (b) With varied cross-coupling coefficients  $\gamma_t$ ,  $\gamma_r \in [0, 0.4]$  (when  $f_r = 5f_s$ ,  $Q_{\text{Tx}} = Q_{\text{Rx}} = 330$ ,  $Q_{\text{Rp}} = 100$ ). (c) With varied self-resonance frequencies  $f_{r\text{Tx}}$ ,  $f_{r\text{Rx}} \in [1.05, 20]f_s$  (when  $Q_{\text{Tx}} = Q_{\text{Rx}} = 330$ ,  $Q_{\text{Rp}} = 100$ ,  $\gamma_t = 0.02$ ,  $\gamma_r = 0.1$ ).

The tolerance on load-dependent phase variation is decided by practical design requirements. For instance, if the inverter has a less stringent requirement on the load impedance angle, the phase-variation tolerance of  $10^\circ$  can be used. This sets a design boundary for the Tx coil self-resonance frequency, as indicated by the green-shaded area.

### B. WPT LINK EFFICIENCY DISCUSSION REGARDING PARASITIC EFFECTS

Finally, the WPT link efficiency is analyzed based on the three types of parasitic parameters, shown in Fig. 8.

It can be observed from Fig. 8(a) that as the quality factor increases, its effect on efficiency improvement becomes less significant.  $Q_{\text{Rx}}$  variations have a similar effect on efficiency as the  $Q_{\text{Tx}}$  variation, so it is not shown in the figure. To obtain the WPT link efficiency higher than 90%, the quality factors  $Q_{\text{Tx}}$  and  $Q_{\text{Rp}}$  should fall within the green-shaded area in Fig. 8(a), which suggests a minimum quality factor of 90 for each coil.

On the other hand, the region of high efficiency considering the effects of cross-couplings  $M_{c\text{Tx}}$  and  $M_{c\text{Rx}}$  also locates around the relation following (16). The load-independence and high-efficiency requirements establish similar boundaries on the cross-couplings, shown as Fig. 8(b).

Considering the WPT efficiency range  $> 90\%$ , the variation range of coil self-resonance frequencies is relatively wide. The self-resonance frequency for the Tx coil  $f_{r\text{Tx}} > 1.28f_s$  and for the Rx coil  $f_{r\text{Rx}} > 1.2f_s$  would already provide  $\eta_{\text{WPT}} > 90\%$ . In contrast, efficiency drops dramatically outside of this range, which should be carefully avoided during design. Therefore, the boundaries for  $f_{r\text{Tx}}$  and  $f_{r\text{Rx}}$  are primarily determined by the requirements for load-independence discussed in the previous Section IV-A.

### C. SYSTEM SETUP AND BOUNDARIES FOR PARASITIC PARAMETERS

In Section II-A, we established boundaries for coil structures based on the magnetic field strengths in poloidal and toroidal directions, while in Sections IV-A and IV-B, we analyzed seven limitations for coil parasitic parameters to ensure a load-independent Rx voltage and WPT link efficiency higher

**TABLE 3.** Boundaries for the Coil Dimension Parameters and the Parasitic Parameters

Requirements on mutual couplings and confined fields		
$\frac{n_{\text{Tx}}n_{\text{Rp}}D_{\text{Tx}}^2}{h_{\text{Tx}}} \geq 6$		$n_{\text{Rp}} \geq 16$
Requirements on efficiency and load-independent output		
$Q_{\text{Tx}} \geq 150$	$\frac{\gamma_r}{\gamma_t} = \frac{mM_{\text{Rx}}}{M_{\text{Tx}}}$	$f_{r\text{Tx}} \geq 4f_s$
$Q_{\text{Rp}} \geq 75$		$f_{r\text{Rp}} \geq f_s$
$Q_{\text{Rx}} \geq 120$		$f_{r\text{Rx}} \geq 3.5f_s$

**TABLE 4.** Parameters of the Coils

	$L$ ( $\mu\text{H}$ )	$M$ ( $\mu\text{H}$ )	$f_r$ (MHz)	$C_p$ (pF)	$Q$	$\gamma$
Tx	4.2	1.44	26.09	10.63	324	0
Rp	9.78		11.93	19.92	95	—
Rx	5.81	1	25.36	7.56	275	0.33 at $45^\circ$ * 0.07 at $90^\circ$ *

\*  $45^\circ$  or  $90^\circ$  represents the rotational gap between two Rxs.

than 90%. Considering the WPT link efficiency and the load-independence within  $1 \pm 5\%$  variation, the coil dimensions and parasitic parameters are defined, as shown in Table 3. Based on the specified boundaries, the WPT link structure is designed according to the dimensions provided in Table 2. The circuit parameters and parasitic parameters of Tx, Rp, and Rx coils are measured as Table 4, which also stays within the design boundaries.

Considering the cross-coupling mutual inductance between the Rx coils, the  $M_{c\text{Rx}}$  values with regard to different coil dimensions (i.e., variation of center-to-center distance  $d_{\text{Rx}} = \frac{D_{\text{Rp}} + D_{\text{Rp}}}{2}$  and Rx-to-Rx angle) are measured as curves in Fig. 9. Higher center-to-center distance and larger Rx-to-Rx gap tend to provide smaller cross-coupling effects. Comparing to the Rp–Rx mutual inductance  $M_{\text{Rx}}$ , the cross-coupling  $M_{c\text{Rx}} < 0.16M_{\text{Rx}}$  is considered acceptable for achieving a load-independent output, see Fig. 6. Therefore, with a  $45^\circ$  rotational gap between two Rxs, the center-to-center distance needs to be higher than 13.5 cm, while there is no limitation on  $d_{\text{Rx}}$  when the Rx rotational gap is  $90^\circ$ .

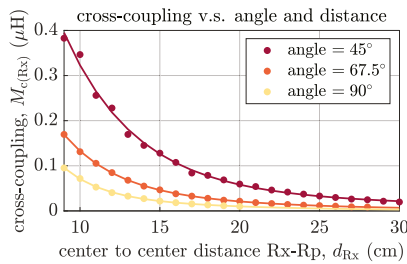


**FIGURE 9.** Rx–Rx cross-coupling with respect to the distance to the center of the Rp and the rotational angle between two Rxs.

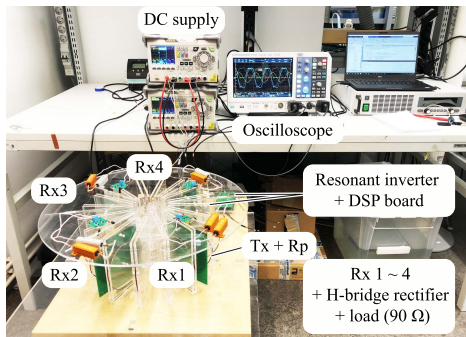


**FIGURE 10.** Experimental setup.

Following the design guidelines, it is suggested to minimize the Rx–Rx cross-couplings to a reasonable range (i.e.,  $M_{cRx} < 0.16M_{Rx}$  in this design example), where the  $M_{cRx}$  effect on Rx independency can be considered negligibly small. However, there are always possibilities or design situations where the parasitic effects in the system are dominant and unavoidable. In some applications, there might be stricter requirements on a constant Rx output voltage. In these cases, for the purpose of performance improvement, the independent control from the Rx-side works perfectly as an alternative and simple solution to compensate the cross-coupling effect and realize the desired power control of the Rx. Such individual control can be easily implemented to the proposed system using conventional methods, without any need for communications between the Tx and Rx devices, e.g., CV control algorithms with dc–dc converters [30], [31] or with active rectifiers [32].

Similarly, the system can also be scaled regarding different full-load Rx-devices amounts or different power levels. The coil dimensions of such WPT systems can be easily redesigned following the guidelines given in this section, by taking notice to design the parasitic parameters inside the valid range and keeping the circuit components inside their safe operation range.

### V. EXPERIMENTAL SETUP AND MEASUREMENTS

In this section, an experimental setup for the multiple receiver WPT system is built, as shown in Fig. 10. The setup consists of a push-pull resonant inverter, four diode-bridge rectifiers, and the proposed WPT link, which is designed following the analysis and guidelines given in Section II-A. The control signals for the inverter are generated by a digital signal processor (DSP) *TMS320F28379*, and each receiver is

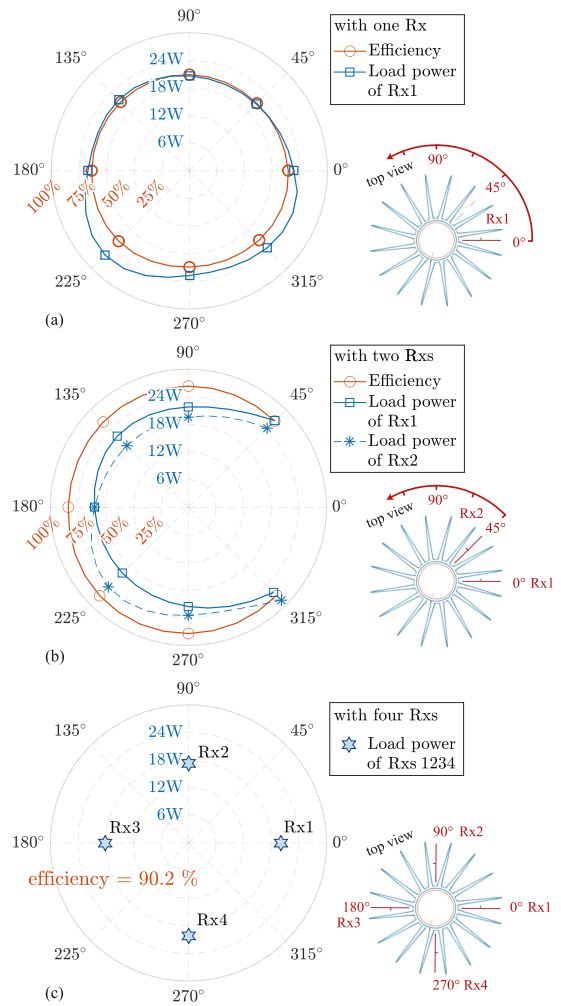


**FIGURE 11.** Measurement result of the dc load power and the system efficiency with (a) only one Rx, and (b) two Rxs rotating around the structure center, and (c) four Rxs.

connected to a rectifier and finally loaded by a  $90\ \Omega$  resistor. Four receiver devices (each containing an Rx coil together with the tuning capacitors, a rectifier, and a load resistance) are used as an example for the full-load case. First of all, the full Rx-rotational freedom is tested with one receiver (Rx1) rotating around the Tx–Rp structure, the measured load power and the system dc-to-dc efficiency are given in Fig. 11(a). The Rx1 load power is almost constant at around 21 W from  $0^\circ$  to  $360^\circ$  rotation, the slight  $P_{Load}$  variation to 26 W at  $225^\circ$  is due to some manufacture asymmetry, while the efficiency for 20-W-level power transfer is maintained at around 70 % at all angles, regardless of the small variation in power.

Next, the rotational freedom is examined with two Rxs in the system: Rx1 is fixed at  $0^\circ$  position, while Rx2 is moved around the Tx–Rp structure. As shown in Fig. 11(b), limited by the Rp structure, the minimum gap between two receivers is tested at  $45^\circ$ . At each Rx2 rotational position, the load powers of Rx1 and Rx2 are measured and recorded as square and star, respectively, in Fig. 11(b). Since Rx1 is fixed at  $0^\circ$  position, its load power is kept almost constant around

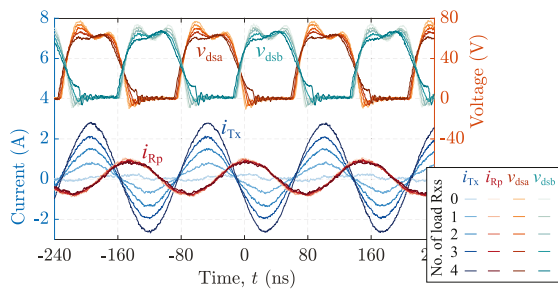


**FIGURE 12.** Experimental waveforms of converter drain-source voltages  $v_{dsa,b}$ , transmitter current  $i_{tx}$ , and repeater current  $i_{rp}$  with regard to system load variations (from zero-load to full-load).

21 W during Rx2 rotation when the cross-coupling effect is negligibly small (i.e., Rx2 from  $90^\circ$  to  $270^\circ$ ). The load power of Rx1 only slightly increased to 26 W at  $45^\circ$  and  $315^\circ$  Rx2-positions, when the cross-coupling between Rx1 and Rx2 is around  $0.32M_{Rx}$ , as seen from Fig. 9.

On the other hand, when the Rx1–Rx2 cross-coupling effects are not significant, the load power of Rx2 follows the same variation trend, as shown in Fig. 11(a). The same power increase happens at around  $225^\circ$  position which verifies that the difference comes from manufacture asymmetry. Similar to the power increase in Rx1, at  $45^\circ$  and  $315^\circ$  rotational positions, the load power in Rx2 also increases slightly due to the increase in  $M_{CRx}$ . The dc-to-dc efficiency of the WPT system with 40-W load is already around 89 %.

Finally, the system reached a dc-to-dc efficiency of 90.2 % with all four Rx loads. The received power at each receiver device (Rx1,2,3,4) is marked with stars in Fig. 11(a). Due to parasitic effects, the power in each Rx load drops slightly from around 21 W to around 18 W, when the load voltage  $V_{rec}$  changes by 7 %. The main waveforms for the converter and the WPT link are also shown in Fig. 12 to validate the working principle of the proposed system. From zero-load to full-load, the Rp coil always maintains a CC, which is solely dependent on the supply voltage. The increase of system power during the load increment is indicated by the Tx current, which exhibits a growing amplitude and constant phase. On the inverter side, the power switches for push and pull legs maintain zero-voltage (ZVS) soft-switching during the load variation, and zero-voltage-derivative switching (ZDS) is reached at the full-load case.

## VI. CONCLUSION

In this article, we proposed a novel structure for multiple-receiver WPT device with a confined field. The transmitter together with the repeater structure can generate a strong and confined magnetic field distributed within a toroidal loop, which greatly enhances coupling to receivers and reduces the leakage flux problem. A 80-W WPT system with four receiver devices is built as an example to demonstrate the proposed concept. The test system provides 90.2 % dc-to-dc efficiency at full load and provides independent constant power transfer around 20 W for each receiver channel.

## REFERENCES

- [1] Z. Yuan, M. Saeedifard, C. Cai, Q. Yang, P. Zhang, and H. Lin, "A misalignment tolerant design for a dual-coupled LCC-S-compensated WPT system with load-independent CC output," *IEEE Trans. Power Electron.*, vol. 37, no. 6, pp. 7480–7492, Jun. 2022.
- [2] J. H. Kim et al., "Plane-type receiving coil with minimum number of coils for omnidirectional wireless power transfer," *IEEE Trans. Power Electron.*, vol. 35, no. 6, pp. 6165–6174, Jun. 2020.
- [3] Z. Zhang and B. Zhang, "Angular-misalignment insensitive omnidirectional wireless power transfer," *IEEE Trans. Ind. Electron.*, vol. 67, no. 4, pp. 2755–2764, Apr. 2020.
- [4] S. Wu, C. Cai, X. Liu, W. Chai, and S. Yang, "Compact and free-positioning omnidirectional wireless power transfer system for unmanned aerial vehicle charging applications," *IEEE Trans. Power Electron.*, vol. 37, no. 8, pp. 8790–8794, Aug. 2022.
- [5] S.-Y. Kim, N.-R. Kwon, S.-H. Ahn, and W.-S. Lee, "Three-dimensional wireless power transfer system using multiple orthogonal resonators for spatial freedom," *IEEE Trans. Antennas Propag.*, vol. 71, no. 5, pp. 4036–4044, May 2023.
- [6] T. Feng, Y. Sun, Y. Feng, and X. Dai, "A tripolar plane-type transmitter for three-dimensional omnidirectional wireless power transfer," *IEEE Trans. Ind. Appl.*, vol. 58, no. 1, pp. 1254–1267, Jan./Feb. 2022.
- [7] H. Liu, Y. Wang, H. Yu, F. Wu, and P. Wheeler, "A novel three-phase omnidirectional wireless power transfer system with zero-switching-loss inverter and cylindrical transmitter coil," *IEEE Trans. Power Electron.*, vol. 38, no. 8, pp. 10426–10441, Aug. 2023.
- [8] K. Lee and S. H. Chae, "Comparative analysis of frequency-selective wireless power transfer for multiple-Rx systems," *IEEE Trans. Power Electron.*, vol. 35, no. 5, pp. 5122–5131, May 2020.
- [9] X. Gao, B. Du, Y. Zhang, and S. Cui, "A dual-frequency compatible wireless power transfer system with a single transmitter and multiple receivers," *IEEE Access*, vol. 10, pp. 102564–102574, 2022.
- [10] Y. Xiao, C. Liu, Y. Huang, and S. Liu, "Concurrent wireless power transfer to multiple receivers with additional resonant frequencies and reduced power switches," *IEEE Trans. Ind. Electron.*, vol. 67, no. 11, pp. 9292–9301, Nov. 2020.
- [11] J.-H. Cho, S. Jung, and Y.-J. Kim, "Wireless power transfer for variable load, distance, and power division ratio in a loosely-coupled multiple-receiver relay system," *IEEE Trans. Ind. Electron.*, vol. 70, no. 7, pp. 6809–6818, Jul. 2023.
- [12] T. Feng, Z. Zuo, Y. Sun, X. Dai, X. Wu, and L. Zhu, "A reticulated planar transmitter using a three-dimensional rotating magnetic field for free-positioning omnidirectional wireless power transfer," *IEEE Trans. Power Electron.*, vol. 37, no. 8, pp. 9999–10015, Aug. 2022.
- [13] J. Feng, Q. Li, F. C. Lee, and M. Fu, "LCCL-LC resonant converter and its soft switching realization for omnidirectional wireless power transfer systems," *IEEE Trans. Power Electron.*, vol. 36, no. 4, pp. 3828–3839, Apr. 2021.
- [14] J. Feng, Q. Li, F. C. Lee, and M. Fu, "Transmitter coils design for free-positioning omnidirectional wireless power transfer system," *IEEE Trans. Ind. Inform.*, vol. 15, no. 8, pp. 4656–4664, Aug. 2019.
- [15] W. M. Ng, C. Zhang, D. Lin, and S. Y. Ron Hui, "Two- and three-dimensional omnidirectional wireless power transfer," *IEEE Trans. Power Electron.*, vol. 29, no. 9, pp. 4470–4474, Sep. 2014.
- [16] H. Wang, C. Zhang, Y. Yang, H. W. R. Liang, and S. Y. R. Hui, "A comparative study on overall efficiency of two-dimensional wireless power transfer systems using rotational and directional methods," *IEEE Trans. Ind. Electron.*, vol. 69, no. 1, pp. 260–269, Jan. 2022, doi: 10.1109/TIE.2020.3048317.
- [17] Z. Zhu et al., "Efficiency optimization and power allocation of omnidirectional wireless power transfer for multiple receivers," *IEEE Trans. Ind. Electron.*, vol. 70, no. 10, pp. 9689–9699, Oct. 2023.
- [18] P. Jayathurathnage, X. Dang, C. R. Simovski, and S. A. Tretyakov, "Self-tuning omnidirectional wireless power transfer using double-toroidal helix coils," *IEEE Trans. Ind. Electron.*, vol. 69, no. 7, pp. 6828–6837, Jul. 2022.
- [19] N. Ha-Van, Y. Liu, P. Jayathurathnage, C. R. Simovski, and S. A. Tretyakov, "Cylindrical transmitting coil for two-dimensional omnidirectional wireless power transfer," *IEEE Trans. Ind. Electron.*, vol. 69, no. 10, pp. 10045–10054, Oct. 2022.
- [20] Y. Gu, J. Wang, Z. Liang, Y. Wu, C. Cecati, and Z. Zhang, "Single-transmitter multiple-pickup wireless power transfer: Advantages, challenges, and corresponding technical solutions," *IEEE Ind. Electron. Mag.*, vol. 14, no. 4, pp. 123–135, Dec. 2020.

- [21] S. A. Al Mahmud, I. Panhwar, and P. Jayathurathnage, "Large-area free-positioning wireless power transfer to movable receivers," *IEEE Trans. Ind. Electron.*, vol. 69, no. 12, pp. 12807–12816, Dec. 2022, doi: 10.1109/TIE.2022.3144591.
- [22] H. Zhang, Y. Shao, N. Kang, H. Qin, C. Ma, and M. Liu, "A vertically modularized reconfigurable wireless power transfer system: Architecture, modeling, and design," *IEEE Trans. Power Electron.*, vol. 38, no. 2, pp. 2730–2742, Feb. 2023.
- [23] S. Li and C. C. Mi, "Wireless power transfer for electric vehicle applications," *IEEE Trans. Emerg. Sel. Topics Power Electron.*, vol. 3, no. 1, pp. 4–17, Mar. 2015.
- [24] J. Song, M. Liu, and C. Ma, "Analysis and design of a high-efficiency 6.78-MHz wireless power transfer system with scalable number of receivers," *IEEE Trans. Ind. Electron.*, vol. 67, no. 10, pp. 8281–8291, Oct. 2020.
- [25] M. Fu, T. Zhang, X. Zhu, P. C.-K. Luk, and C. Ma, "Compensation of cross coupling in multiple-receiver wireless power transfer systems," *IEEE Trans. Ind. Inform.*, vol. 12, no. 2, pp. 474–482, Apr. 2016.
- [26] "AirFuel alliance resonant wireless power transfer (WPT) system baseline system specification (BSS)," AirFuel Alliance, Beaverton, OR, USA, AFA TS-0010-A v2.00, Jul. 2018.
- [27] Y. Shao, M. Liu, and C. Ma, "A multi-receiver MHz WPT system with hybrid coupler," in *Proc. IEEE PELS Workshop Emerg. Technol.: Wireless Power Transfer*, 2021, pp. 1–6.
- [28] K. N. Surakitbovorn and J. M. Rivas-Davila, "On the optimization of a class-E power amplifier with GaN HEMTs at megahertz operation," *IEEE Trans. Power Electron.*, vol. 35, no. 4, pp. 4009–4023, Apr. 2020.
- [29] Y. Liu, P. Jayathurathnage, and J. Kyyrä, "A new simplified method and design guidelines for the optimization of push–pull class  $\Phi_2$  converters for wireless power transfer applications," *IEEE Trans. Power Electron.*, vol. 38, no. 8, pp. 10442–10459, Aug. 2023.
- [30] J. Feng, Q. Li, and F. C. Lee, "Load detection and power flow control algorithm for an omnidirectional wireless power transfer system," *IEEE Trans. Ind. Electron.*, vol. 69, no. 2, pp. 1422–1431, Feb. 2022.
- [31] M. Fu, H. Yin, M. Liu, Y. Wang, and C. Ma, "A 6.78 MHz multiple-receiver wireless power transfer system with constant output voltage and optimum efficiency," *IEEE Trans. Power Electron.*, vol. 33, no. 6, pp. 5330–5340, Jun. 2018.
- [32] M. Liu, J. Song, and C. Ma, "Active class E rectifier for DC output voltage regulation in megahertz wireless power transfer systems," *IEEE Trans. Ind. Electron.*, vol. 67, no. 5, pp. 3618–3628, May 2020.



**YINING LIU** received the B.Sc. and M.Sc. degrees in electrical engineering from the Harbin Institute of Technology (HIT), Harbin, China, in 2018 and 2020, respectively. She is currently working toward the doctoral degree in electrical power and energy engineering with the Department of Electrical Engineering and Automation, School of Electrical Engineering, Aalto University, Espoo, Finland.

Her research interests include wireless power transfer, high-frequency power converters, soft-switching converters, and wide-bandgap devices.



**NAM HA-VAN** (Member, IEEE) received the B.S. degree in electronics and telecommunications engineering from the School of Electronics and Telecommunications, Hanoi University of Science and Technology, Hanoi, Vietnam, in 2012, and the Ph.D. degree in information and telecommunication engineering from Soongsil University, Seoul, South Korea, in 2019.

From 2019 to 2020, he was a Postdoctoral Researcher with Soongsil University. From 2020 to 2023, he was a Postdoctoral Researcher with the

Department of Electronics and Nanoengineering, School of Electrical Engineering, Aalto University, Espoo, Finland, where he is currently a Research Fellow with the Department of Electrical Engineering and Automation, School of Electrical Engineering. His research interests include wireless power transfer, electromagnetic theory, metamaterials, antennas, and energy harvesting systems.



**PRASAD JAYATHURATHNAGE** (Senior Member, IEEE) received the B.Sc. degree in electronics and telecommunications engineering from the University of Moratuwa, Moratuwa, Sri Lanka, in 2009, and the Ph.D. degree in electrical and electronic engineering from Nanyang Technological University, Singapore, in 2017.

From 2017 to 2018, he was a Research Fellow with the Queensland University of Technology, Brisbane City, QLD, Australia, and Rolls-Royce-NTU Corporate Lab, Singapore. From 2018 to

2023, he was a Full-Time Postdoctoral Researcher with the School of Electrical Engineering, Aalto University, Espoo, Finland, and an Academic Guest with the Power Electronic Systems Laboratory, ETH Zurich, Zurich, Switzerland. He is currently a Senior Research Engineer with Danfoss Drives, Tampere, Finland, and continues his academic affiliation with Aalto University as an Academic Visitor. He has authored more than 60 research articles in various journals, conferences, and tutorial seminars. His research interests include high-frequency power converters, wide-band-gap devices, passive components, and wireless power transfer.

Dr. Jayathurathnage was the recipient of several accolades for his research, including the Best Paper Awards at IEEE International Power Electronics and Motion Control Conference 2018, IEEE International Symposium on Medical Information and Communication Technology 2019, and IEEE Annual Southern Power Electronics Conference 2022.



**JORMA KYYRÄ** (Member, IEEE) received the M.Sc., Lic.Sc., and D.Sc. degrees in electrical engineering from the Helsinki University of Technology (TKK), which is currently Aalto University, Helsinki, Finland, in 1987, 1991, and 1995, respectively.

Since 1985, he has been in various positions with Aalto University, where he has been an Associate Professor of Power Electronics, since 1996, and a Professor of Power Electronics, since 1998. From 2008 to 2009, he was the Dean of the Faculty of

Electronics, Communications and Automation, TKK. From 2009 to 2011, he was the Vice President of Aalto University, where he is currently the Head of the Department of Electrical Engineering and Automation. The power electronics group at Aalto University has expertise, such as in power electronics for ac drives, dc–dc converters, modeling of converters, filtering of EMI, power factor correction, and distributed power systems. His research interest includes power electronics at large.



**SERGEI A. TRET'YAKOV** (Fellow, IEEE) received the Diploma Engineer-Physicist, Candidate of Sciences (Ph.D.), and D.Sc. degrees in radiophysics from Saint Petersburg State Technical University, Saint Petersburg, Russia, in 1980, 1987, and 1995, respectively.

From 1980 to 2000, he was with the Department of Radiophysics, Saint Petersburg State Technical University. He is currently a Professor of Radio Science with the Department of Electronics and Nanoengineering, Aalto University, Espoo, Finland. He has authored or coauthored six research monographs and over 350 journal articles. His research interests include electromagnetic field theory, complex media electromagnetics, metamaterials, and microwave engineering.

Dr. Tret'yakov served as the Chairman of the Saint Petersburg IEEE Electron Devices/Microwave Theory and the Techniques/Antennas and Propagation Chapter, from 1995 to 1998, and the General Chair of the International Congress Series on Advanced Electromagnetic Materials in Microwaves and Optics (Metamaterials) and the President of the Virtual Institute for Artificial Electromagnetic Materials and Metamaterials (Metamorphose VI), from 2007 to 2013.